

## An experimental investigation into the drag reduction performance of dimpled plates in a fully turbulent channel flow

İlter, Yasin Kaan; Ünal, Uğur Oral; Shi, Weichao; Tokgöz, Sedat; Atlar, Mehmet

**DOI**

[10.1016/j.oceaneng.2024.118198](https://doi.org/10.1016/j.oceaneng.2024.118198)

**Publication date**

2024

**Document Version**

Final published version

**Published in**

Ocean Engineering

**Citation (APA)**

İlter, Y. K., Ünal, U. O., Shi, W., Tokgöz, S., & Atlar, M. (2024). An experimental investigation into the drag reduction performance of dimpled plates in a fully turbulent channel flow. *Ocean Engineering*, 307, Article 118198. <https://doi.org/10.1016/j.oceaneng.2024.118198>

**Important note**

To cite this publication, please use the final published version (if applicable). Please check the document version above.

**Copyright**

Other than for strictly personal use, it is not permitted to download, forward or distribute the text or part of it, without the consent of the author(s) and/or copyright holder(s), unless the work is under an open content license such as Creative Commons.

**Takedown policy**

Please contact us and provide details if you believe this document breaches copyrights. We will remove access to the work immediately and investigate your claim.



## Research paper

# An experimental investigation into the drag reduction performance of dimpled plates in a fully turbulent channel flow

Yasin Kaan İlter<sup>a,b,\*</sup>, Uğur Oral Ünal<sup>b</sup>, Weichao Shi<sup>c</sup>, Sedat Tokgöz<sup>d</sup>, Mehmet Atlar<sup>a</sup>

<sup>a</sup> University of Strathclyde, Glasgow, United Kingdom

<sup>b</sup> Istanbul Technical University, Istanbul, Turkey

<sup>c</sup> Newcastle University, Newcastle, United Kingdom

<sup>d</sup> Delft University of Technology, Delft, Netherlands

## ARTICLE INFO

## Keywords:

Drag reduction

Dimpled surfaces

Fully turbulent flow channel

Skin friction reduction

## ABSTRACT

Dimpled surfaces have gained increasing attention in recent years for their potential to reduce turbulent skin friction, a capability previously acknowledged for its beneficial implications on heat transfer. As a passive drag reduction method, dimpled surfaces offer significant advantages for marine applications due to their effectiveness and practical applicability. However, despite numerous studies, conflicting opinions and inconsistent drag reduction rates persist in the literature. This paper addresses these ambiguities and offers valuable insights into the effectiveness of dimpled surfaces for drag reduction in fully turbulent flows. We conducted an extensive experimental investigation involving various dimple configurations, including different depth-to-diameter ratios, diameters and orientations, utilising a specialised Fully Turbulent Flow Channel facility and a Particle Image Velocimetry system. Our findings demonstrated that circular dimple geometries, particularly those with low depth ratios, can achieve significant drag reduction of up to 27% as the Reynolds number increases. These results highlight the substantial potential of dimpled surfaces for improving energy efficiency in marine applications, where skin friction accounts for a significant portion of the total drag experienced by large vessels.

## 1. Introduction

In order to achieve zero carbon targets and meet rigorous emission-reduction regulations, the development of effective drag-reducing technology and techniques has become an essential area in recent years. Skin friction influences a considerable component of the total drag encountered by seagoing platforms such as ships and submarines during their operation. Because of their massive size and high operational speeds, these platforms produce turbulent boundary layers, making reducing turbulent skin friction a priority for enhancing energy efficiency and reducing environmental impact. As a result, there is a growing interest in researching creative technologies that can successfully minimise skin friction while also contributing to overall emission reductions in the maritime industry.

Among the various drag reduction techniques, passive methods have gathered significant attention due to their simplicity, cost-effectiveness, and potential for long-term energy savings. Passive drag reduction methods, such as surface modifications and textured coatings, aim to manipulate the flow and reduce skin friction without requiring active

input or energy consumption. One promising passive drag reduction approach that has been extensively studied in recent years is the use of circular dimple geometries. While dimpled surfaces have been primarily investigated for their heat transfer enhancement capabilities (Afanasyev et al., 1993; Burgess and Ligrani, 2005; Chen et al., 2012), there is now a growing interest in exploring their potential as a passive drag-reducing method, particularly due to their ability to modulate the turbulent boundary layer.

Dimpled surfaces have emerged as a potent passive solution for maritime applications, given their extensive potential for skin friction reduction and practical applicability (Alekseev et al., 1998; van Nesselrooij et al., 2016; Vida, 2004). The effectiveness of dimpled surfaces in reducing drag was first discovered by researchers in 1998, who demonstrated that shallow dimples could decrease drag in fully turbulent flow by up to 20% despite the increase in the form drag component (Alekseev et al., 1998). This ground-breaking finding opened up new avenues for research into the drag-reduction capabilities of dimpled surfaces. However, the efficacy of dimpled surfaces in reducing drag has not been consistently observed, as evidenced by a study in 2008 where

\* Corresponding author. University of Strathclyde, Glasgow, United Kingdom.

E-mail addresses: [ykilter@itu.edu.tr](mailto:ykilter@itu.edu.tr), [kaan.ilter@strath.ac.uk](mailto:kaan.ilter@strath.ac.uk), [kaanilter@gmail.com](mailto:kaanilter@gmail.com) (Y.K. İlter).

<https://doi.org/10.1016/j.oceaneng.2024.118198>

Received 25 January 2024; Received in revised form 13 May 2024; Accepted 13 May 2024

Available online 20 May 2024

0029-8018/© 2024 The Authors. Published by Elsevier Ltd. This is an open access article under the CC BY license (<http://creativecommons.org/licenses/by/4.0/>).

researchers reported no drag reduction in their trials (Lienhart et al., 2008). These conflicting results highlight the need for further investigation into the fundamental mechanisms underlying the drag reduction performance of dimpled surfaces and the optimisation of dimple geometries for specific applications.

Some researchers claim that the inconsistent results reported in the literature can be attributed to the drag-reducing effect only happening in turbulent flows (Tay, 2016; Tay et al., 2015). A patent holder for the dimpled technologies contends that drag reduction only happens in turbulent flows and claims that up to 34% drag reduction is possible (Vida, 2004). Using circular dimples, "Tornado Like Technology (TLT)" is a drag-reduction method that was introduced in 2004 (Wüst, 2004). It is stated that the dents on the surface of an object will generate tornado-like vortices that reduce the drag. This article involves the unique industrial application of dimpled surfaces, which are applied on a high-speed train model. The paper, however, did not provide any scientific background about the drag-reduction mechanisms of the dimples. Consequently, several dimple investigations were performed using solely flat walls with regular arrays of spherical dimples due to the complexity of the physical mechanism. A group of researchers mentioned retained energy levels at larger scales, which imply greater streamwise coherence and stability of the flow (Tay et al., 2015). In addition to the freestream flow conditions, the flow over the dimples is influenced by various dimple parameters. The most significant of these parameters is the dimple depth. Previous studies showed that the drag increases as the dimple depth-to-diameter ratio increases (Burgess and Ligrani, 2005). Flow separation is observed for the dimples with depth-to-diameter ratios greater than 10%. Separated flow creates pressure drag and lacks the gain on the wall shear stress. However, some studies focused on flow structures with depth-to-diameter ratios greater than 20% to see dynamic flow structural characteristics (Ligrani et al., 2001; Turnow et al., 2012). Also, some studies indicate that the drag reduction only occurred with coverage ratios higher than 70% (Tay, 2011; Wu and Yeo, 2011). Furthermore, the orientation of the dimple pattern has a significant impact. Recent experimental studies on the physical mechanism of the effect of dimples on the boundary layer flow argue that the drag reduction effect is related to the strong dependency on pattern orientation and dimple geometry (Tay et al., 2015; van Nesselrooij et al., 2016). These studies have investigated the relationship between energy cascade, vorticity, and dimple pattern in the context of drag reduction. Tay et al. (2015) conducted direct numerical simulations (DNS) of shallow dimples in channel flow. They observed that dimples induce spanwise flow components, disrupting the normal energy cascade process in turbulent flows. They found that this disruption reduces turbulent energy production and stabilizes the flow, ultimately resulting in decreased skin friction drag. Similarly, van Nesselrooij et al. (2016) experimentally studied the drag reduction effects of dimpled surfaces in turbulent boundary layers. They noted that the dimples influence the streamwise vorticity, which acts to reduce skin friction drag. They suggested that the spanwise flow components induced by the dimples interfere with the typical energy cascade mechanism, leading to reduced turbulent energy production and a more stable flow. Furthermore, they have shown that the fundamental flow characteristics and drag reduction mechanisms associated with dimpled surfaces remain consistent across a wide range of Reynolds numbers. It is worth noting that a more recent study, which was published after the completion of the experimental work presented in this paper, showed that diamond-like dimple patterns can reduce mean drag by 7.4%. In comparison, circular dimples increased by approximately 6% (Ng et al., 2020). Although this study provides valuable insights into the comparative performance of different dimple geometries, it was not available when conducting the experiments described herein. Nevertheless, the findings of Ng et al. (2020) underscore the importance of exploring various dimple shapes and configurations to optimise their drag reduction potential. They also serve as a valuable reference point for future research in this field.

Building upon the existing body of research on dimpled surfaces, it is important to consider the flow conditions under which these studies have been conducted. A significant portion of the literature on dimpled surfaces has focused on fully developed channel flows, which are widely known as wall-bounded flows. These flows provide a relatively simple and well-defined environment for the verification and evaluation of theoretical models (Andrade et al., 2018; Hussain and Reynolds, 1975; Kim et al., 1987; Laufer, 1951; Moser et al., 1999). By investigating the performance of dimpled surfaces in fully developed channel flows, researchers can gain valuable insights into the fundamental mechanisms governing drag reduction and develop a deeper understanding of how dimple geometries interact with the turbulent boundary layer. However, it is crucial to recognize that the findings from these studies may not directly translate to more complex flow conditions encountered in real-world applications, such as those found in the maritime industry. Therefore, while fully developed channel flow studies serve as an essential foundation for understanding the drag-reduction capabilities of dimpled surfaces, further research is needed to bridge the gap between these simplified flow conditions and the practical implementation of dimpled surfaces in marine environments.

The above review highlights that dimple patterns have great potential as a passive drag-reducing solution. At the same time, highly conflicting views and drag reduction rates are still reported in the literature, and there is a lack of information about the frictional drag reduction mechanism. The primary objective of the present paper is to assess the efficacy of dimpled surfaces in reducing drag force in fully turbulent flow conditions representative of real-life ship scale applications. By conducting experimental studies on various dimple configurations, including different depth-to-diameter ratios, diameters, and orientations, we aim to elucidate the mechanisms underlying drag reduction and explore the practical applicability of dimpled surfaces for marine transportation. Furthermore, we intend to provide insights into the relationship between dimple geometry, flow characteristics, and drag reduction effectiveness. Within the framework of the study, various dimple depth-to-diameter ratios and different dimple arrangements and geometries with coverage ratios higher than 85% were considered. Experimental pressure drop and PIV measurements were conducted in the fully turbulent flow channel facility (FTFC) of the University of Strathclyde. The drag results obtained from the experimental studies were recalculated by correction factors using numerical studies of İltter et al. (2023), assuming that the effects obtained at low Reynolds numbers based on the channel height and mean bulk velocity ( $Re_H$ ) will be similar at high  $Re_H$  numbers. The drag changes calculated based on pressure drop measurements showed similarity with numerical results obtained for low  $Re_H$  numbers. The paper emphasises the large potential of the dimpled structures in terms of drag reduction.

## 2. Model geometries and experimental setup

The experimental studies were conducted on flat and dimpled plates in a fully turbulent flow channel, FTFC, located at the Kelvin Hydrodynamic Laboratory of the University of Strathclyde. The three-dimensional visual of the test section, along with the inlet and outlet sections of FTFC are given in Fig. 1. An overall visual of the setup can be seen in Fig. 2. The primary characteristics of the channel are provided in Table 1. The Reynolds number,  $Re_H$ , is calculated based on the channel height and the bulk velocity.

In the flow channel, average velocity is measured using a flow meter that can calculate the volumetric flow rate. Also, the pressure drop obtained from the pressure sensors located at the contraction section and the pitot tube located immediately after the test section can be used to calculate both average and centreline velocities. The hydrodynamic performance of the plates is determined by measuring the pressure drop along the length of the plate. This is done using six pressure taps and one pressure sensor placed on the side wall of the test section. The numbering of the pressure taps can be found in Fig. 3.



Fig. 1. 3D CAD representation of the testing section of the FTFC.



Fig. 2. A general view of the FTFC, left: control unit and visual access side of the FTFC, right: pump outlet and contraction pressure tap side of the FTFC.

Table 1  
Technical specifications of the FTFC.

Upstream length:	2.40	m
Test section length:	0.600	m
Channel width:	0.18	m
Channel height:	0.0225	m
Speed range:	1.0–13.5	m/s
$Re_{Hf}$ :	~20,000–350,000	

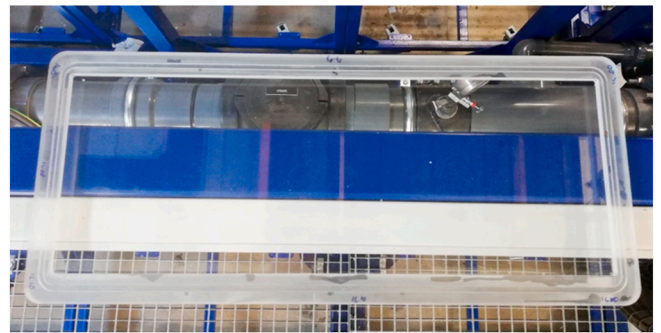


Fig. 4. Reference clear acrylic plate.

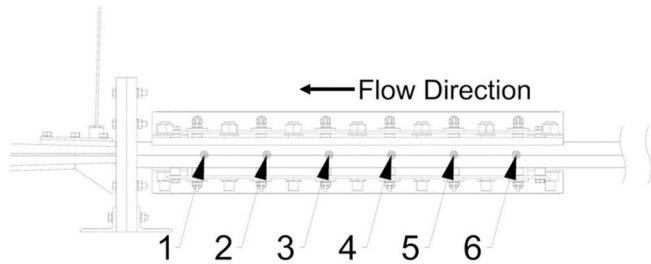


Fig. 3. Pressure tap numbering and flow direction along the test section.

Test plates can be mounted on the bottom and top walls of the channel. The opposite side wall of the test section, facing the pressure measurement points, is designed with an observation window suitable for laser use. An acrylic transparent test plate can also be used on the bottom or top wall of the channel for laser-assisted measurements. A picture of the reference acrylic flat plate used in the tests is provided in Fig. 4.

Bolted frame interfaces mount the plates on the bottom and top walls. This allows for control over plate alignment with the channel surface during plate changes. Any differences that may arise from plate

mounting can be minimised by using a torque wrench for assembly. The bottom plate's position (flushness) control can be performed before placing the top plate. The position of the top plate (flushness) can be checked using the steel frame used for mounting before putting it on the test section.

The selection of circular dimples for our experimental studies was based on the prevailing literature. The choice of diameters 45 mm, 60 mm, and 90 mm for the dimpled plates was influenced by the dimensions of the FTFC. Furthermore, our manufactured dimpled plates' geometric characteristics and Reynolds numbers were carefully selected to cover a range of dimple configurations and Reynolds number regimes relevant to real-life applications. Considering the corresponding boundary layer thickness around midship for a 100-m-long tanker, the selected diameter range represents 500 mm–900 mm dimple structures on the ship hull. The geometric characteristics and Reynolds numbers of the manufactured dimpled plates are provided in Table 2. Fig. 5 represents the sections of the dimple geometries. Figs. 6–9 display examples

**Table 2**  
Technical details of the manufactured dimpled plates.

	$D45_4/D45_{4sg}$	$D90_4$	$D60_6$	$D45_8$	$D90_6$	$D60_8$	$D60_3$
$\delta/d$	6.25	3.13	3.13	3.13	2.08	2.34	6.25
$d/D$	4.0%	4.0%	6.0%	8.0%	6.0%	8.0%	3.0%
$d$ [mm]	1.800	3.600	3.600	3.600	5.400	4.800	1.800
$D$ [mm]	45.00	90.00	60.00	45.00	90.00	60.00	60.00
$Re_D$ (min)	44,821	89,641	59,761	44,821	89,641	59,761	59,761
$Re_D$ (max)	627,490	1,254,980	836,653	627,490	1,254,980	836,653	836,653

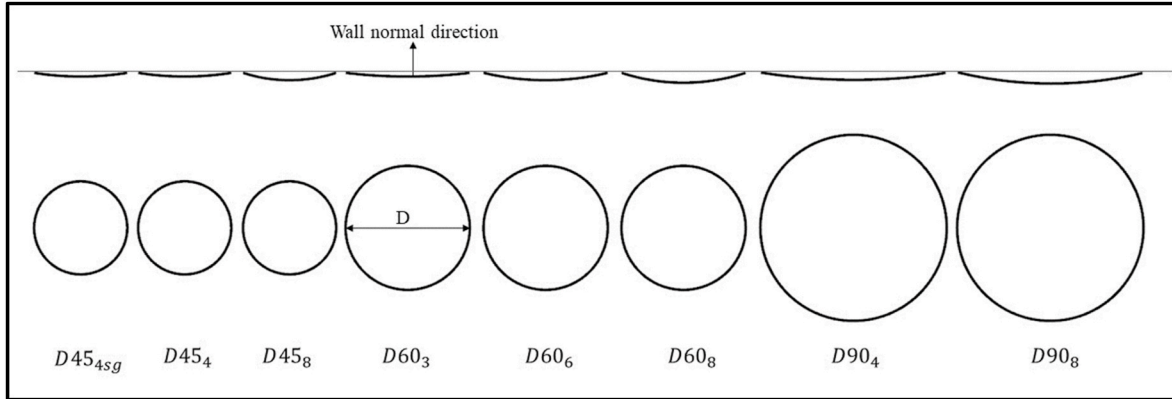


**Fig. 5.** Cross section (top) and top views (bottom) of the dimple geometries. The grey solid line represents the test section's zero plane (flat surface level).

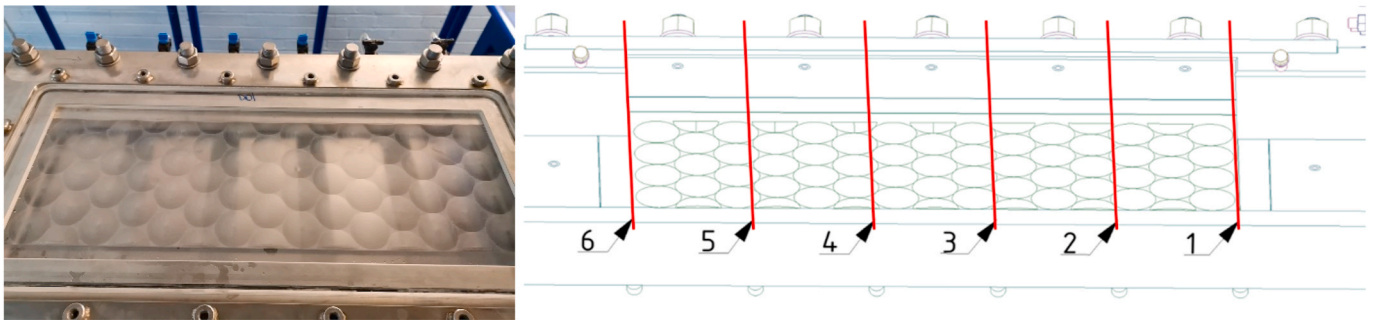


**Fig. 6.**  $D45_{4sg}$  representation: Acrylic plate photo (left) and 3D-CAD representation with pressure tap projections (right). The flow direction is from left to right.

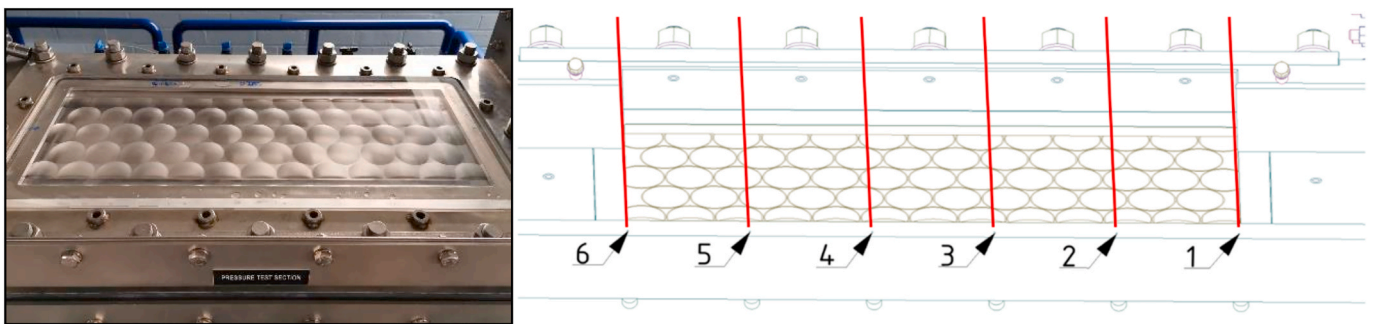


**Fig. 7.**  $D45_4$  and  $D45_8$  representation: Acrylic plate photo (left) and 3D-CAD representation with pressure tap projections (right). The flow direction is from left to right.

of the tested manufactured plates and a 3D-CAD representation of the plate in the test section. The CAD view also includes projections of the pressure taps, which indicate the relative location of each dimple structure to the pressure measurement points.  $Re_D$  represents the Reynolds number based on the dimple diameter and considering the FTFC's velocity range. This parameter allows us to characterise the flow around

dimples specifically and compare our results with existing literature that may use similar non-dimensional parameters.

In channel flow experiments, non-dimensional Reynolds numbers, such as Reynolds numbers based on channel height and bulk velocity,  $Re_H$  and  $Re_D$ , are commonly used to characterise flow conditions and compare results across different studies. These non-dimensional

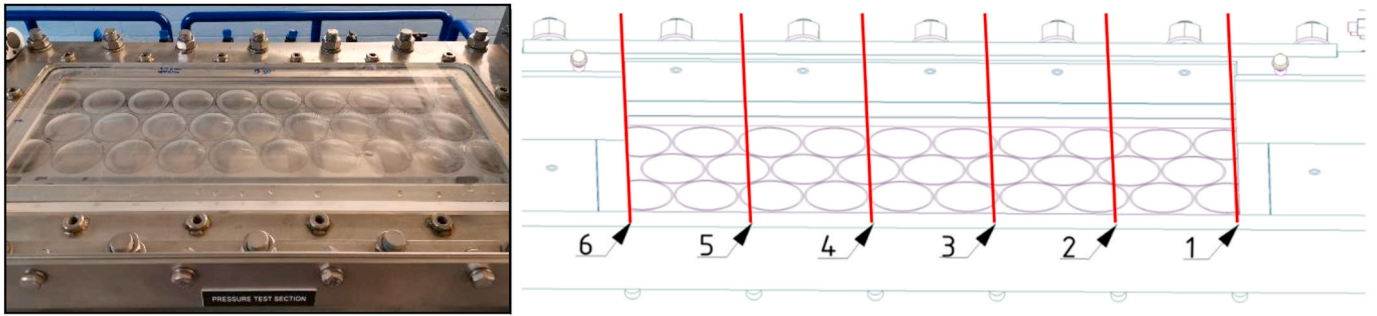


Fig. 8.  $D60_8$  and  $D60_3$  representation: Acrylic plate photo (left) and 3D-CAD representation with pressure tap projections (right). The flow direction is from left to right.

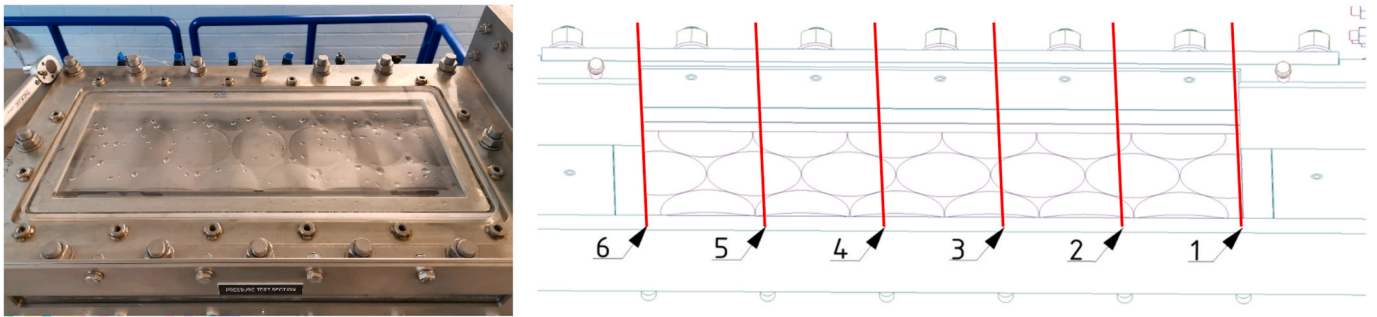


Fig. 9.  $D90_4$  and  $D90_6$  representation: Acrylic plate photo (left) and 3D-CAD representation with pressure tap projections (right). The flow direction is from left to right.

numbers offer insights into the flow regime and are essential for understanding fluid dynamics. However, introducing additional non-dimensional parameters tailored to the particular geometry or flow configuration is often beneficial in studies focusing on specific features, such as dimpled surfaces. By utilising Reynolds numbers based on the dimple parameters, such as  $Re_D$ , we aim to provide results consistent with those reported in the literature, facilitating comparisons and ensuring compatibility with existing research findings. These non-dimensional parameters complement traditional flow descriptors and offer a more detailed understanding of the flow characteristics near dimpled surfaces within the context of channel flow experiments.

### 3. Pressure drop measurement and methodology

#### 3.1. Data collection

The FTFC system uses an in-house developed LabView system for data acquisition and processing. During the tests, the average sampling frequency of the data collection system was 100 Hz. Considering the total measurement durations, the number of samples was determined as 10,000. The total measurement period approximately corresponded to a time interval of 100 s.

The pressure differences obtained from both pairs of pressure taps were used to determine the drag characteristics of the plates placed in the test section. The skin friction coefficient can be found using equations (3.1) and (3.2) by half channel height.

$$C_f = \tau_w / (0.5 \rho U_b^2) \quad (3.1)$$

$$\tau_w = - \frac{H \Delta P}{2 \Delta x} \quad (3.2)$$

where  $H$  is the channel height in  $m$ ,  $\tau_w$  is wall shear stress in  $N/m^2$ ,  $\rho$  is fluid density in  $kg/m^3$ ,  $U_b$  is mean bulk velocity in  $m/s$ ,  $\Delta P$  is the pressure difference in Pa, and  $\Delta x$  is the distance between pressure

measurement points in  $m$ .

The Reynolds number based on the mean bulk velocity can be calculated as follows.

$$Re_H = \rho U_b H / \mu \quad (3.3)$$

where  $\mu$  implies the dynamic viscosity of the fluid in  $kg/(m \cdot s)$ . The recommended procedures of the International Towing Tank Conference (ITTC) were utilised to determine corresponding freshwater properties for different temperatures (26th ITTC Specialist Committee on Uncertainty Analysis, 2011).

The facility was first calibrated based on the study conducted by Marino et al. (2020). The calibration measurements were taken using hydraulically smooth test panels. The variation of the skin friction coefficients depending on the Reynolds number is depicted in Fig. 10. The solid and dashed black lines in the graph represent the skin friction resistance coefficient curves proposed by Dean and Zanoun, respectively (Dean, 1978; Zanoun et al., 2003).

Fig. 10 shows that, for the smooth plates, the results obtained from pressure tap pairs 1–3, 1–4, 1–5, 1–6, 2–3, and 2–6 align more closely with the reference curves.

For the dimpled plates, to minimise interactions between the dimple shapes and the pressure taps, it was decided to compare the measurements taken from the 1–6 tap pair, which has the longest measurement distance. Since different configurations of dimple structures exhibit variability in their relative positions to the pressure taps, conducting the examinations through the 1–6 tap pair was deemed a more reliable approach.

During the data collection, measurements were repeatedly taken from different tap configurations. The average bulk velocity obtained from these repetitions was highly consistent depending on the pump frequency. Fig. 11 shows that overlapping measured velocities against pump frequency. Each point contains 15–20 overlapped measurements.

Similar to the velocity measurements, consistent results were obtained in the repeated pressure drop measurements. At least three

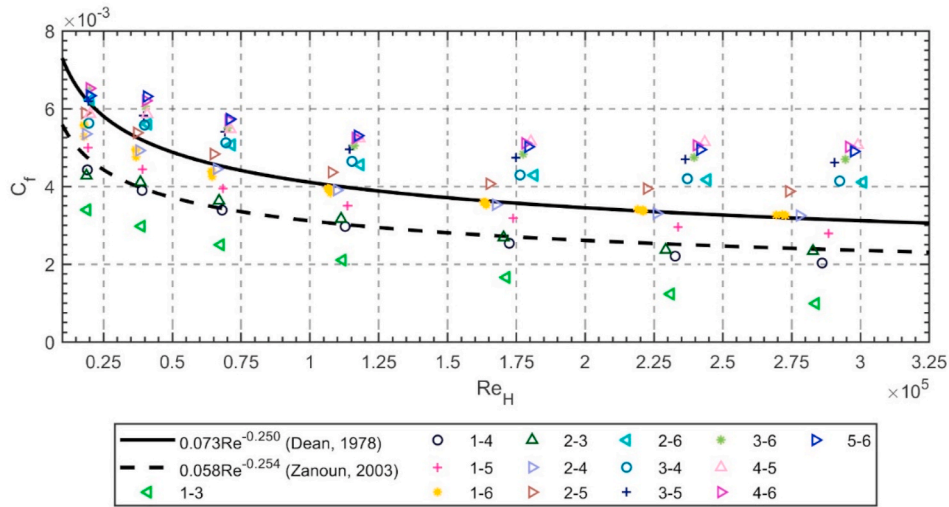


Fig. 10. Skin friction coefficient variations for different tap configurations.

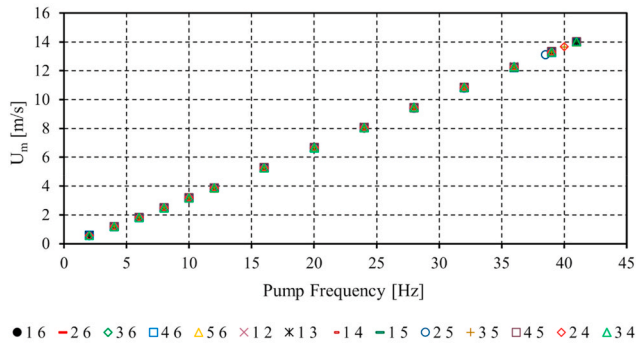


Fig. 11. Mean bulk velocities against pump frequency for different tap configurations.

repeated measurements were taken for each velocity. The results for the 1–6 tap pair are provided in Fig. 12, which includes the related curves from the literature, as an example of the consistency of the results.

3.2. Uncertainty analysis

Repeated pressure drop tests were performed to conduct an uncertainty analysis for the flat plate measurements. The analysis involved 11 or more repetitions at different speeds, using pressure differences corresponding to a constant pump frequency. Due to temperature variations

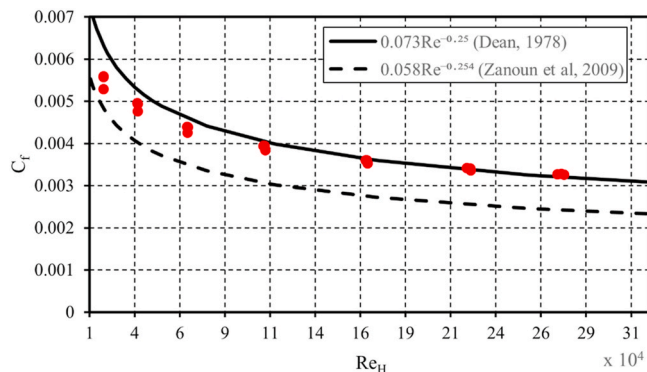


Fig. 12. Skin friction coefficient against  $Re_H$  for 1–6 pressure tap configuration, red dots represent measurements.

during measurements taken at various times, the calculated Reynolds numbers varied. Considering the temperature differences, the calculated uncertainties are expected to be even lower if pressure differences corresponding to the same Reynolds numbers were used. The uncertainty analysis in this study adhered to the principles outlined by Coleman and Glenn Steele (1995), and the coefficients for a 95% confidence interval were obtained from their study. The calculated percentage values of combined standard uncertainty,  $b_c$ , are presented in Table 3. The total systematic measurement error is estimated to be 1%. This comprehensive uncertainty analysis ensures the reliability and robustness of the flat plate measurements, providing a solid foundation for the subsequent analysis and comparison with the dimpled plate configurations.

Two separate uncertainty analyses were performed on two plates with the smallest and largest diameters for dimpled plates. On plate D01 (D45<sub>4</sub>), repeated measurements were taken without stopping the pump or removing and reconnecting the pressure tap hoses. On plate D02 (D90<sub>4</sub>), the hose positions were changed before each measurement, and measurements were taken by stopping and restarting the pump. Calculated uncertainties on pressure drop measurements for both cases are given in Table 4.

3.3. Data correction procedure

The pressure drop measurements for the flat plate were successfully completed without any issues, as the flow reached two-dimensional continuity at each measurement section. However, the pressure drop measurements taken over dimpled plates required redefinition. The dimpled plates introduced a third dimension to the flow in the test section, deviating from typical fully developed channel flow behaviour. Data from the reference flat plate measurements and computational fluid dynamics (CFD) studies of dimpled structures were utilised to accurately evaluate the pressure drop measurements on dimpled plates. The raw data was recalculated using correction coefficients derived from low-velocity CFD studies and subsequently incorporated into the evaluation. Processing the raw data without correction would lead to the erroneous conclusion that dimpled structures, including those with a

Table 3  
Uncertainty analyses for the flat plate pressure drop measurements.

Pump Freq. [Hz]	Pressure Tap Configuration	$b_c$ [%]
16 (~5 m/s)	ΔP @ 1-6	2.2
10 (~3 m/s)	ΔP @ 1-6	2.0
39 (~13 m/s)	ΔP @ 1-6	1.3

**Table 4**  
Uncertainty analyses for the dimpled plates pressure drop measurements.

Pump Freq. [Hz]	Pressure Tap Configuration	Plate	$b_c$ [%]
16 (~5 m/s)	1-6	D01	1.0
6 (~2 m/s)	1-6	D02	1.0
32 (~11 m/s)	1-6	D02	1.1

depth-to-diameter ratio of 8%, provide benefits in the 10–30% range. This discrepancy highlights the necessity of applying appropriate corrections to the raw measurements to ensure accurate analysis and interpretation of the results.

Method validation was first carried out to calculate the correction coefficients based on measurements performed on the flat plate and previous CFD results (İltter et al., 2023). In the experimental setup, the skin friction coefficient is an indirectly calculated parameter based on pressure drop measurements rather than a directly measurable value. Conversely, variables such as wall shear stress, skin friction, and pressure are directly measurable within computational fluid dynamics (CFD) simulations. It was observed that the results obtained from skin friction coefficient calculations performed using pressure data from CFD were consistent with those obtained using experimental methods. Based on this finding, a two-step correction process was applied to the raw measurements for dimpled plates. First, correction factors were derived from the deviation ratios between values calculated using the experimental method and those directly measured within CFD, such as wall shear stress and total drag variables. Second, an additional correction was performed to account for the volumetric changes in the test section due to the presence of dimple structures. The resulting overall correlation coefficients are presented in Table 5. This correction process ensures that the experimental results accurately reflect the impact of dimple structures on the skin friction coefficient, considering both the limitations of indirect measurement and the geometric changes introduced by the dimples.

The average skin friction coefficients of the plates were calculated using Equation (3.1), based on the measured pressure differences. However, it is crucial to acknowledge that dimpled plates in a channel flow introduce a form drag component in addition to skin friction resistance. The  $C_f$  calculation in Equation (3.1) is only valid for situations where the form drag effect is absent, necessitating a correction for dimpled plates. The correction factors provided in Table 5 were applied to the  $\Delta P$  values to account for this additional drag component. Due to the scope of the numerical study, pressure drop corrections could only be performed for the configurations  $D45_4$ ,  $D45_{4sg}$ ,  $D45_8$ ,  $D60_8$ , and  $D60_3$ .

To calculate the total drag forces accurately, the shear stress values on the plate surface were first computed using Equation (3.2) and then multiplied by the respective surface areas of the plates to obtain the corresponding force values. These force values were then adjusted using the correction coefficients from Table 5 to incorporate the form drag contribution. This approach ensures that the calculated total drag forces accurately reflect the combined effects of skin friction and form drag induced by the dimpled plates in the channel flow.

**Table 5**  
Pressure drop correction coefficients determined based on the previously conducted CFD study (İltter et al., 2023).

Case	Correction Factor
$D45_{4sg}$	1.24
$D45_4$	1.21
$D45_8$	2.15
$D60_8$	2.08
$D60_3$	1.09

#### 4. PIV measurements

The flow visualisation measurements were conducted in the Fully Turbulent Flow Channel (FTFC) of the University of Strathclyde, outlined in the previous sections by using a two-dimensional Particle Image Velocimetry (PIV) measurement system. The imaging system included the "New Wave Gemini" dual-pulse laser device to illuminate the seeding particles. The laser system comprises a laser-generating head, two control modules, and two power sources. The generator head contains two distinct laser sources, each with a maximum operating frequency of 15 Hz. Although the system has a power capacity of 120 mJ, satisfactory readings were achieved by operating it within the power range of 30%–40%. The measurements were performed at a frequency of 12.5 Hz. The image recording equipment consists of a high-speed Photron Fastcam Mini camera unit equipped with a 60 mm Nikon F2.8 lens and a resolution of  $1280 \times 1024$  pixels. The time between laser pulses was calculated individually for various flow velocities. It was ensured that, in all instances, the displacement of the seeding particles between image pairs remained within the range of three to five pixels.

DaVis PIV software was used for the pre- and post-processing of the measurements. The software allowed the configuration of the key settings related to the sampling rate, camera data bandwidth, calibration information, laser pulse frequency, etc. It synchronised the camera and laser frequencies with the aid of a synchroniser to capture image pairs with precise timing. Once image acquisition was complete, cross-correlation algorithms and vector calculations were applied to the raw images, ultimately generating velocity vector fields. The software also managed to store the raw and processed image data output by the camera.

Silver-coated hollow glass sphere particles with a diameter of  $13 \mu\text{m}$  supplied by HART Materials were used as the seeding material. The particles had a silver content of 20% by mass and an average density of  $1.6 \text{ g/cc}$ . The reflective silver coating on the spherical particles enabled their effective visualisation and tracking during the PIV imaging. The small  $13 \mu\text{m}$  diameter of the particles ensured they accurately followed the flow with minimal slip. The near-neutral density of  $1.6 \text{ g/cc}$  also allowed the particles to be suspended uniformly within the flow field.

##### 4.1. Measurement system and image processing procedure

To accurately calibrate the PIV system, it is necessary to establish the actual distance in the real world corresponding to the displacement of pixels in the image frame. In order to help with this calibration, a metal ruler was placed in the channel to serve as a reference object with predetermined dimensions. The dimple sizes for the trials involving plates were confirmed to be consistent with the intended values, which facilitated the calibration procedure by giving length scales within the frame. After the calibration, the PIV measurements were performed on a plane parallel to the test plate. The measurements were taken at a distance of  $y^*/H = 0.35$  from the channel base. Here,  $y^*$  represents the distance from the channel base, and the zero plane is defined at the level of the flat plate. The zero plane is shown in Fig. 5. It is important to note that the dimple geometries lie beneath the baseline, meaning that the bottom of the dimple starts from a negative position. By calibrating using length scales within the frame and establishing the height of the measurement plane relative to the non-dimensional channel height  $H$ , the PIV data were accurately scaled from pixels to real-world velocity vectors. A general view of the measurement setup is presented in Fig. 14.

An image pre-processing method consisting of two stages was devised to exclude undesirable background features that could have a detrimental effect on PIV vector calculations. Initially, a 9-pixel sliding subtraction approach was employed to reduce fluctuating background noise caused by the reflections and ambient lighting. Subsequently, a consistent subtraction procedure was employed, utilising a pre-determined density threshold of 900 counts, resulting in a further decrease in the detectability of immobile background structures. The

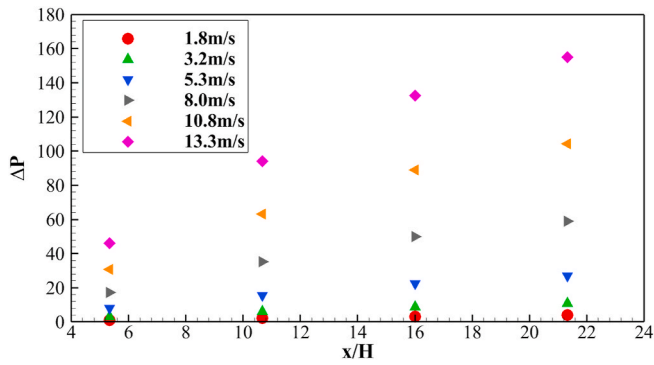


Fig. 13. Pressure drop comparison for different x/H at different pump frequencies.



Fig. 14. General view of the measurement set-up with the PIV system.

initial raw image intensities ranged from 2400 to 4600 counts; however, after the pre-processing stage, the final images had intensity values ranging from 1200 to 1800 counts. The substantial decrease illustrates the efficacy of the sliding and continuous subtraction algorithms in reducing unwanted background items. The pre-treatment step involved removing unwanted elements from the images before doing vector computations. This guaranteed that the correlations between consecutive frames were accurate and not affected by any irrelevant background features. In general, the optimised two-stage technique improved the

quality of the PIV measurements. An example displaying the effect of the pre-processing on the image quality is presented in Fig. 15.

The velocity vectors from the pre-processed images were calculated using a multi-stage PIV algorithm. The image frames were divided into interrogation windows comprised of one  $64 \times 64$  pixels area and three  $16 \times 16$  pixels sub-areas. Careful seeding ensured adequate particle densities within these interrogation windows for robust vector calculations. The laser power was adjusted to optimise the reflection intensities from the silver-coated seeding particles. A 50% overlap between the adjacent interrogation windows was utilised to minimise errors from window edge effects and loss of particle pairs near query borders. The multi-stage approach with optimised seeding densities, reflection intensities, and overlap helped improve the accuracy and resolution of the final velocity vector fields derived from the PIV measurements.

Outliers may need to be filtered out within the vector fields obtained from PIV images. Various algorithms exist for cleaning and correcting these bad vectors (Raffel et al., 2018). In this study, the Universal Outlier Detection algorithm, a development of the median test for detecting and removing bad vectors, was employed (Westerweel and Scarano, 2005). Subsequently, the vectors were calculated by averaging the surrounding vectors to fill in the deleted bad vectors.

The time-averaged flow variables were calculated as a final step by taking the temporal averages of the calculated instantaneous 1024 vector fields. Fig. 16 provides a comparison of the final velocity distributions obtained with and without using the sliding subtraction and constant density subtraction algorithms for illustrative purposes. Comparisons are given for the case of  $D45_s$ , which most affects the average flow. The applied algorithms are highly effective in correcting defective areas without causing significant changes in velocity distributions.

#### 4.2. Average vector field uncertainty analysis

The location of each velocity vector in the averaged fields was determined using equation (4.1).

$$\bar{x} = \frac{1}{N} \sum_{i=1}^N x_i \tag{4.1}$$

where  $N$  is the number of samples at each location,  $x_i$  is the instantaneous  $u$  or  $v$  velocity component, and  $\bar{x}$  is the mean  $u$  or  $v$  value. The standard deviation ( $\sigma_x$ ) of each velocity component ( $u, v$ ) at each vector location was calculated to quantify the fluctuations in the PIV measurements.  $\sigma_x$  was determined using equation (4.2):

$$\text{var}(x) \equiv \sigma_x^2 = \frac{1}{N-1} \sum_{i=1}^N (x_i - \bar{x})^2 \tag{4.2}$$

Both vector fields contain  $N$  vectors for each location and each variable function. When calculating uncertainty for mean values, the

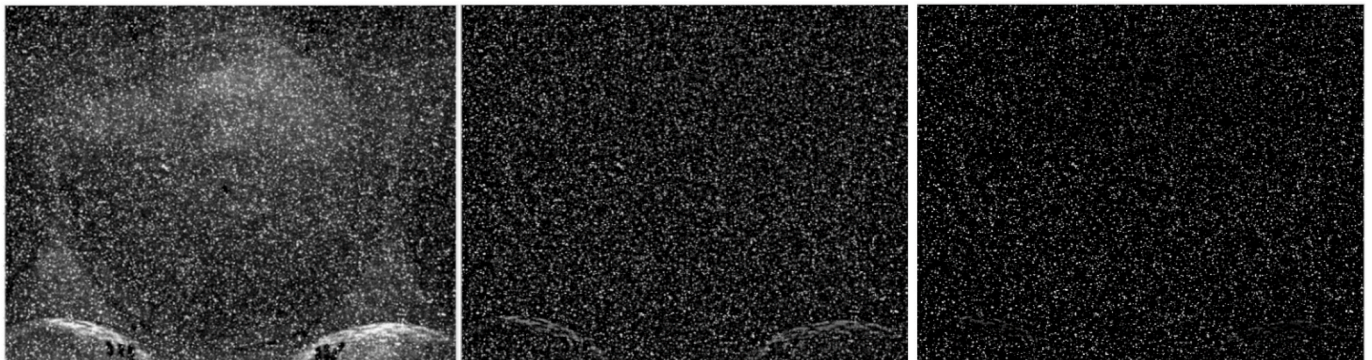
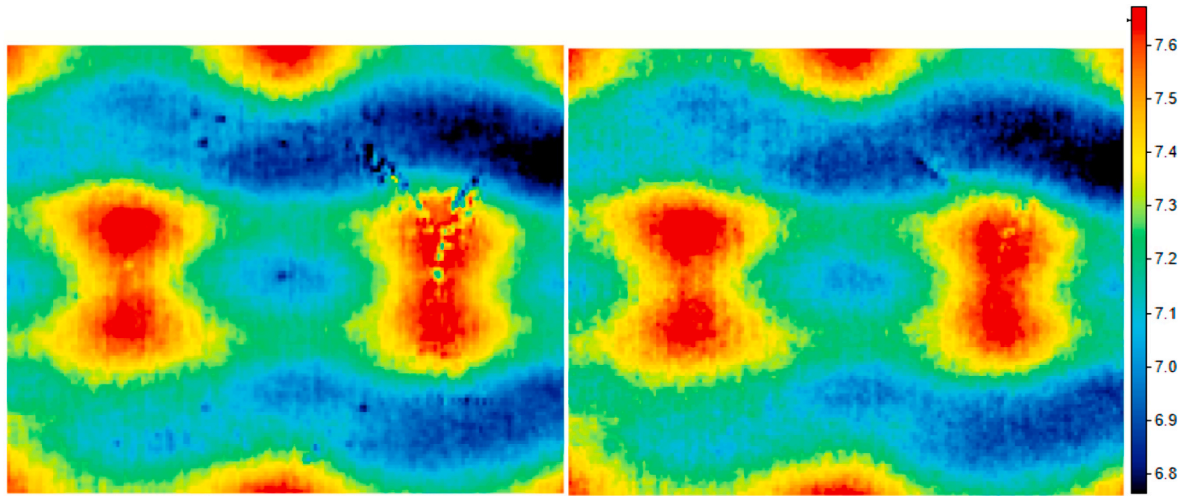


Fig. 15. Pre-processing of PIV images for case  $D60_s$ . The leftmost image shows the original raw frame containing background noise. The middle image displays the result after sliding subtraction to reduce variable background effects. The rightmost image shows the final pre-processed result after applying constant density subtraction to minimise stationary background features.



**Fig. 16.** The comparative visuals of the effects of algorithms used in the PIV image processing process on the results. On the left side, the streamwise velocity contours obtained without using the respective algorithms are presented, while on the right side, the contours obtained using the algorithms are shown. The flow direction is from left to right.

standard deviation and the number of vectors are used, as shown in equation (4.3). The uncertainty for each variable  $\bar{x}$  is expressed as  $U_{\bar{x}}$ .

$$U_{\bar{x}} = \sigma_x \sqrt{\frac{1}{N}} \quad (4.3)$$

Similarly, for the uncertainty calculation of the standard deviation, the expression is given in equation (4.4).

$$U_{\sigma_x} = \sigma_x \sqrt{\frac{1}{2(N-1)}} \quad (4.4)$$

If we consider the uncertainty expression for the mean velocity as  $U_{\bar{x}} = U_{\bar{u}} = \sigma_u / \sqrt{N}$ , the standard deviation,  $\sigma_u$ , contains both the real velocity fluctuations ( $\sigma_{u,fluct}$ ) and the measurement errors ( $\sigma_{u,err}$ ). In this case,  $\sigma_{u,err}$  can be expressed as in Equation (4.5):

$$\sigma_u^2 = \sigma_{u,fluct}^2 + \sigma_{u,err}^2 \approx \sigma_{u,fluct}^2 + \bar{U}_u^2 \quad (4.5)$$

here,  $U_u$  represents the uncertainty of the instantaneous velocity component, and the  $\bar{U}_u^2$  term represents the mean square of the  $U_u$  uncertainty term. If the samples are not independent, the  $N$  terms should be replaced with  $N_{eff}$  which represents the effective number of independent samples (Sciacchitano and Wieneke, 2016).

Finally, the calculated uncertainty values are presented by multiplying with a constant  $k$  coefficient to calculate the 95% confidence interval. The confidence interval calculation is given in equation (4.6).

$$I_c = k \times \sigma \quad (4.6)$$

where, the  $k$  value corresponds to 1.960 for the 95% confidence interval. The  $k$  value represents the width of the Gaussian function used. The total integral contains the percentage of data specified by the determined confidence interval. For example, when  $k = 1.96$ , it covers 95% of all values around the centre while leaving out 0.025% at each end.

Table 6 presents the calculated uncertainty values for the averaged  $\bar{u}$  and  $\bar{w}$  velocity components. These are compared to the surface averages of the corresponding components. The uncertainty percentages for  $\bar{u}$  remain below 1%, while  $\bar{w}$  uncertainties are around 50% of the mean. The higher relative uncertainty in  $\bar{w}$  is expected, given the much lower absolute velocities measured compared to  $\bar{u}$ . For example, uncertainties of around 0.024 m/s for  $\bar{u}$  and 0.017 m/s for  $\bar{w}$  components correspond to 0.3% and 20% of the respective mean velocities in the measurement area. This trend holds across different cases. The frequencies in Table 6

**Table 6**

The uncertainty percentages at a 95% confidence interval for PIV average velocity components.

	Freq. [Hz]	$U_b$ [m/s]	$\bar{u}$ [%]	$\bar{w}$ [%]
D45 <sub>4</sub>	6	1.79	0.8	-52.7
D45 <sub>4</sub>	24	8.02	0.8	-49.4
D45 <sub>4</sub>	38	12.85	0.7	-48.1
D45 <sub>4sg</sub>	6	1.79	0.4	-25.3
D45 <sub>4sg</sub>	24	8.02	0.4	-24.6
D45 <sub>4sg</sub>	38	12.85	0.3	-25.1
D60 <sub>6</sub>	6	1.79	0.4	-26.6
D60 <sub>6</sub>	24	8.02	0.4	-25.4
D60 <sub>6</sub>	38	12.85	0.4	-25.0
D45 <sub>8</sub>	6	1.79	1.0	-67.2
D45 <sub>8</sub>	24	8.02	1.0	-59.3
D45 <sub>8</sub>	38	12.85	0.9	-57.8
D60 <sub>8</sub>	6	1.79	0.4	-27.9
D60 <sub>8</sub>	24	8.02	0.4	-26.4
D60 <sub>8</sub>	38	12.85	0.5	-27.1
D60 <sub>3</sub>	6	1.79	0.3	-21.3
D60 <sub>3</sub>	24	8.02	0.3	-20.5
D60 <sub>3</sub>	38	12.85	0.7	-45.3
FP	6	1.79	0.8	-49.8
FP	24	8.02	0.7	-49.3
FP	38	12.85	0.7	-44.5

correspond to approximate mean  $\bar{u}$  velocities of 1.9, 7.5, and 11 m/s, while the bulk velocities  $U_b$  are about 1.79, 8.02, and 12.85 m/s. Overall, the uncertainty analysis provides quantitative error bounds on the PIV measurements relative to the measured velocity magnitudes.

## 5. Results and discussion

### 5.1. Pressure drop measurements

The drag reduction percentages for the investigated cases are presented in Fig. 17. The percentage values are also provided in Table 7 which also includes results obtained from computational studies conducted at low speeds by (İltter et al., 2023). When calculating the percentage differences for the computational studies, the force values were determined by considering the surface projection area of each dimpled plate in relation to the corresponding flat plate area. This approach ensures a fair comparison between the dimpled and flat surfaces, accounting for the potential differences in the surface area.

The experimental results clearly demonstrate that introducing dim-

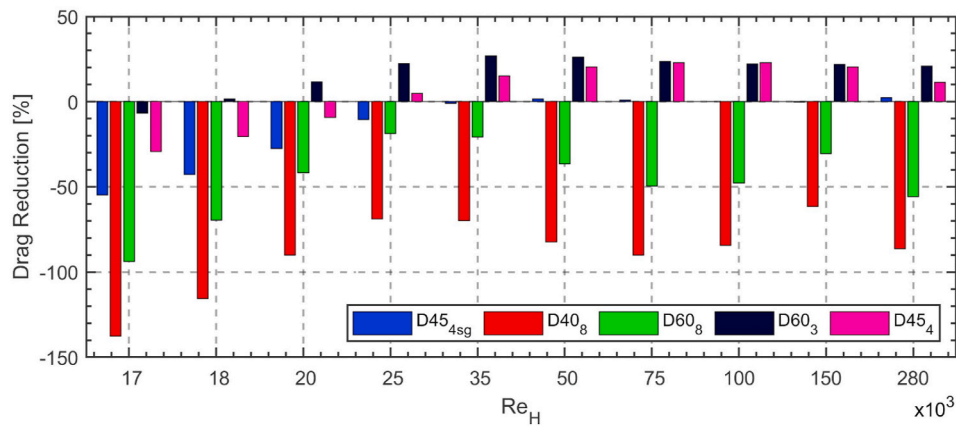


Fig. 17. Drag reduction for dimple configurations against  $Re_H$  (negative values indicate a drag increase).

Table 7

Drag reduction in percentages (%) for different dimple configurations (Negative values indicate a drag increase).

$Re_H$	D45 <sub>4sg</sub>	D45 <sub>8</sub>	D60 <sub>8</sub>	D60 <sub>3</sub>	D45 <sub>4</sub>	Source
2800	-31.4	-115.3	-124.1	-9	-21.5	CFD (İtler et al., 2023)
17,000	-54.7	-137.6	-93.7	-6.7	-29.3	EFD (Present study)
18,000	-42.7	-115.6	-69.6	1.5	-20.5	
20,000	-27.5	-90.1	-41.8	11.7	-9.2	
25,000	-10.6	-68.8	-18.7	22.3	4.8	
35,000	-0.9	-69.8	-20.7	26.8	15.1	
50,000	1.5	-82.3	-36.5	26.1	20.4	
75,000	0.9	-90	-49.4	23.6	22.8	
100,000	0	-84.4	-47.9	22.2	22.7	
150,000	-0.3	-61.6	-30.5	21.8	20.2	
280,000	2.3	-86.3	-55.9	20.7	11.2	

ples can lead to significant energy savings notably for the cases D45<sub>4</sub> and D60<sub>3</sub> exhibiting substantial drag reduction rates of up to 26.8% as the Reynolds number increased. This remarkable finding at high Reynolds numbers suggests that the application of dimple structures could be highly promising in marine environments, where skin friction drag is a dominant component of the total resistance experienced by vessels. Consequently, further investigation into the applicability of dimpled surfaces in maritime contexts is strongly recommended to exploit their potential for energy efficiency improvements fully.

However, it is important to note that the present study’s findings regarding the effectiveness of dimple alignment differ from some previous literature (e.g. Spalart et al., 2019; van Nesselrooij et al., 2016; Veldhuis and Vervoort, 2009). Contrary to these earlier reports, the current experiments indicate that dimpled structures aligned with the flow were more effective in reducing drag than staggered arrangements. In fact, the staggered configurations significantly increased the drag force at relatively low Reynolds numbers. This discrepancy highlights the need for further research to understand the factors influencing the performance of different dimple alignments and to reconcile the conflicting observations.

Furthermore, the experimental results revealed that the dimple geometries with high depth ratios considerably increased drag levels, likely due to their significant form drag component. It is crucial to recognize that the total drag obtained for the flat plates is solely expressed through the frictional resistance component. In contrast, the total drag force on the dimpled surfaces comprises both frictional resistance and form drag. As the Reynolds number based on dimple depth ( $Re_d$ ) increases, the form drag component is expected to rise, potentially leading to flow separations within the dimpled structure. However, the present study found that the effect of  $Re_d$  varies for dimples of different diameters, even when the  $Re_d$  value remains constant. This observation suggests that  $Re_d$  alone should not be considered a definitive parameter for characterising the performance of dimpled surfaces. Instead, the impact of the cross-sectional expansion rate should be considered when analysing the flow behaviour in the centre cross-section of the dimpled structure. These factors will be highly valuable in future studies involving various dimple geometries, as they can guide the design and optimisation of dimpled surfaces for specific applications.

It is also important to emphasise that similar trends in drag reduction were observed at low Reynolds number levels in both the experimental and computational studies, as indicated in Table 7. The agreement between the experimental and numerical findings suggests that dimpled structures can be considered a viable approach for passive drag reduction when studied under controlled parameters in an open-flow setting. This methodology shows promise in maritime applications, particularly in optimising the section shape and arrangement of dimples on vessel hulls. By leveraging the insights gained from this study and further exploring the performance of dimpled surfaces in realistic maritime conditions, researchers can develop effective strategies for reducing skin friction drag and improving the energy efficiency of marine vehicles.

The pressure drop measurements presented in this study provide valuable evidence of the drag reduction potential of dimpled surfaces in turbulent flow conditions. The findings highlight the importance of optimising dimple geometry and alignment to maximise their effectiveness while also revealing the need for further research to address the

discrepancies with previous literature and to explore the applicability of dimpled surfaces in maritime environments. By considering the factors identified in this study and conducting additional investigations, researchers can advance the understanding of dimpled surfaces as a passive drag reduction technique and contribute to developing more efficient and sustainable marine transportation solutions.

#### 5.1.1. Further remarks on enhancing measurement methods

The present experimental study was conducted with a single channel height and, therefore, a single boundary layer thickness. It is crucial to conduct examinations with varying channel heights to gain a more comprehensive understanding of how dimpled structures interact with the boundary layer. By systematically altering the channel height, researchers can investigate the performance of dimpled surfaces under different boundary layer thicknesses. This approach would enable a deeper analysis of the relationship between the boundary layer characteristics and the effectiveness of dimpled surfaces in reducing drag.

As explored in the next section (5.2), in addition to varying the channel height, conducting drag measurements and flow visualisations within the boundary layer at different thicknesses in external flow conditions can provide valuable insights into the effects of dimpled structures. External flow conditions like those encountered in maritime applications often involve more complex boundary layer dynamics than the fully developed channel flow, as studied in the present work. By examining the flow behaviour and drag characteristics within the boundary layer in these external flow conditions, researchers can better understand how dimpled surfaces perform in practical applications. However, it is important to note that ensuring fully developed flow over the dimpled surfaces is a critical aspect of this experimental approach. Fully developed flow conditions are necessary to accurately assess the dimpled surfaces' performance and obtain reliable drag measurements. Achieving fully developed flow requires careful consideration of two key parameters: the length of the test plate and the thickness of the near-wall region within the boundary layer.

The above discussion highlights the need for future experimental studies to investigate the effects of boundary layer thickness on the performance of dimpled surfaces in turbulent flow conditions. By conducting examinations with varying channel heights and exploring the flow behaviour and drag characteristics within the boundary layer in external flow conditions, researchers can better understand how dimpled structures interact with the boundary layer and optimise their design for practical applications. However, ensuring fully developed flow over the dimpled surfaces and striking the right balance between test plate length and boundary layer thickness are critical considerations for the success of this experimental approach.

## 5.2. Time-averaged flow fields

Fig. 18 shows the non-dimensional streamwise velocity distributions for various dimple configurations at 1.79 m/s mean bulk velocity. All dimpled cases showed a decrease in mean velocities in the measurement plane compared to the flat plate case.  $D45_4$  and  $D60_3$  exhibit a single high-speed region around the dimple edges while  $D45_{4sg}$ ,  $D45_8$ , and  $D60_8$  develop symmetric velocity peaks about the centreline. For the staggered  $D45_{4sg}$  case, high-speed corridors form along x-sections at the edges, and low-speed corridors occur through the dimple centre. As

noted, diagonal dimple arrangements produce parallel velocity zones, while parallel arrangements induce diagonal zones, agreeing with prior works in the open literature (van Nesselrooij et al., 2016). Although  $D45_4$  and  $D60_3$  have equal  $Re_d$ , the high-speed region grows with increased dimple size in  $D60_3$ . In  $D60_8$ , velocities drop significantly below  $U_b$  away from the edges while  $D45_8$  has only a local centreline decrease. As discussed earlier, at  $Re_b = 35,000$ ,  $D60_3$ ,  $D45_4$ ,  $D45_{4sg}$  reduce the resistance by 43%, 27% and 7%, respectively. The increased  $\bar{u}$  distribution for  $D60_3$  versus  $D45_4$  correlates to its better drag reduction. Across all velocities studied the cavity-induced velocity distortions agree with previous experimental observations (Tay, 2016; Tay et al., 2015; van Nesselrooij et al., 2016).

Shown in Figs. 19 and 20 are the non-dimensional streamwise velocity distributions at 24 Hz ( $Re_b \cong 16,000$ ;  $U_b \cong 8.0$  m/s) and 38 Hz ( $Re_b \cong 25,000$ ;  $U_b \cong 12.9$  m/s) pump frequencies, respectively. Similar to that observed at 6 Hz pump frequency,  $\bar{u}/U_b$  distributions of the dimpled cases remain at a lower level compared to that of the flat plate. Across the Reynolds numbers investigated, comparable behaviours persist for each dimple case, while the velocity reduction strengthens with increasing  $Re_b$ . The velocity increase has a greater impact on  $D45_{4sg}$ ,  $D45_8$ , and  $D60_8$ . In  $D45_{4sg}$ , the high-speed corridors become more continuous. For  $D45_8$  and  $D60_8$ , the velocity peaks at the edges shift inward. In  $D45_8$ , the low-speed centre region is displaced towards the dimple sides. At 38 Hz, this interacts with the next cavity's low-speed region, akin to  $D45_4$ . At the same speed, the high-speed corridors strengthen for  $D45_{4sg}$ . For the deep  $D45_8$  and  $D60_8$  cavities, cavitation occurs at the edges, causing localised velocity reductions. Cavitation is variable due to the open channel's interaction with the atmosphere. While similar behaviours persist with the Reynolds number, the distortions of the mean velocity fields are enhanced, particularly for  $D45_{4sg}$ ,  $D45_8$ , and  $D60_8$ . Cavitation emerges at higher  $Re_b$  in the deep cavities.

Figs. 21–23 show the non-dimensional transverse velocity distributions at pump frequencies of 6, 24 and 38 Hz, respectively. To improve visualisation,  $\bar{w}$  values for all pump frequencies are 2 times exaggerated for all cases due to very low  $\bar{w}$  values recorded. Examining the velocity distributions in Fig. 21, it is generally observed that, as expected, a symmetric distribution occurs around the centreline. Comparing the cases  $D45_4$  and  $D45_{4sg}$ , it is seen that transverse velocity levels are much higher for the staggered  $D45_{4sg}$  case. For all dimpled structures, it can be easily seen that there is liveliness in the flow towards the centreline due to the dimple effect occurring on the surface. While high  $\bar{w}$  distributions occur at the dimple entrance and exit edge lines for cases  $D45_4$ ,  $D60_3$ ,  $D45_8$ , and  $D60_8$ , for  $D45_{4sg}$  the  $\bar{w}$  area is seen to be shifted from the dimple entrance edge towards the dimple centreline. The high  $\bar{w}$  distributions starting at the dimple entrance edge are seen to persist until the dimple centreline in  $D60_3$ .

For the cases  $D45_8$  and  $D60_8$ , unlike the other dimpled cases, it can be observed that the high/low transverse velocity areas occurring outside the dimple edge lines are connected to the previous and next cavities. For the  $D45_{4sg}$  case, it can be seen that the perpendicular high corridors align parallel to the flow, similar to the  $D45_8$  and  $D60_8$  cases. The transverse flow components of the cases  $D45_4$  and  $D45_{4sg}$  present similar magnitudes to those observed in  $D60_3$ .

The general topology of the flow displayed by the dimpled cases

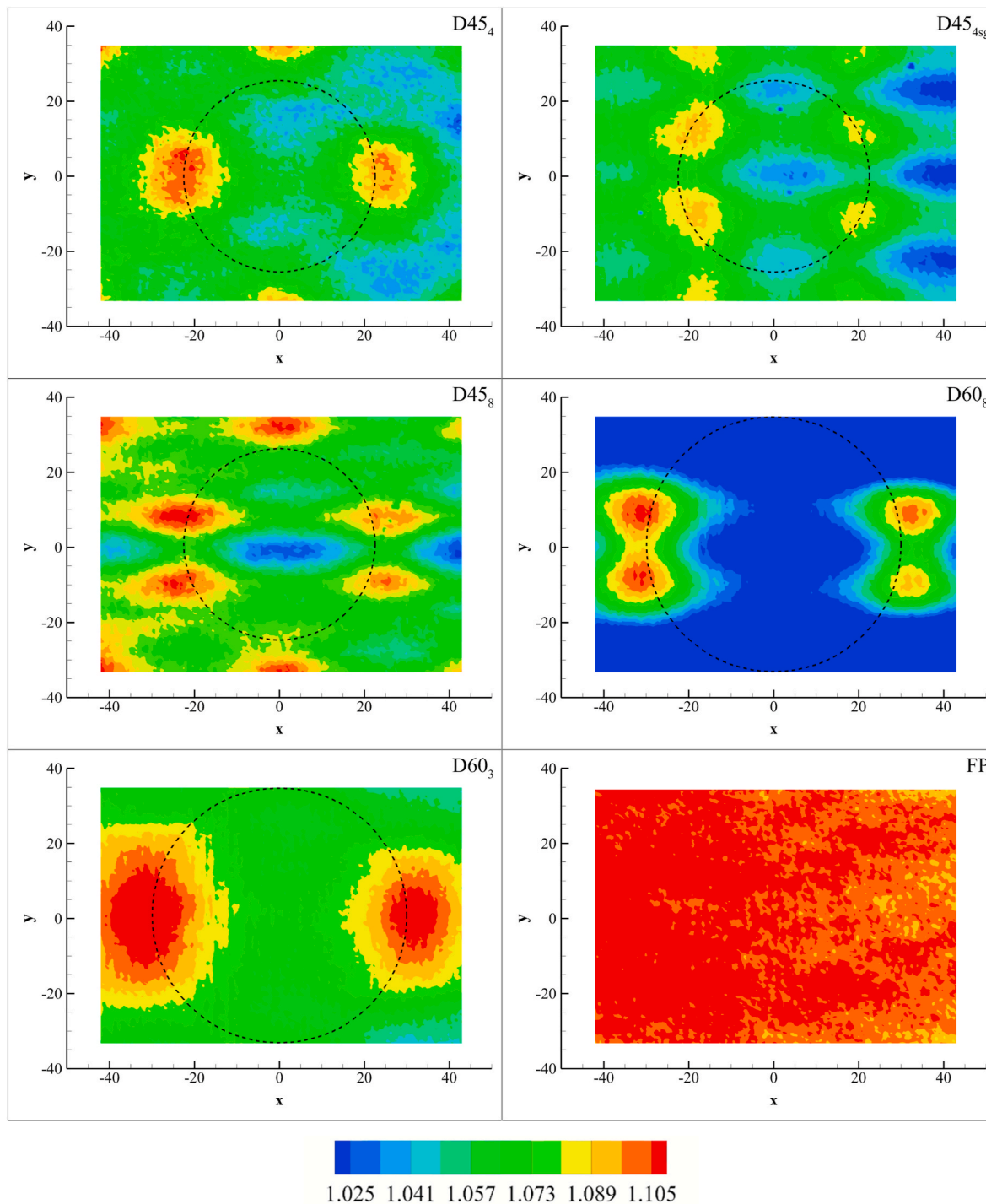


Fig. 18.  $\bar{u}/U_b$  distributions at 6 Hz pump frequency ( $U_b \cong 1.79$  m/s). The flow direction is from left to right.

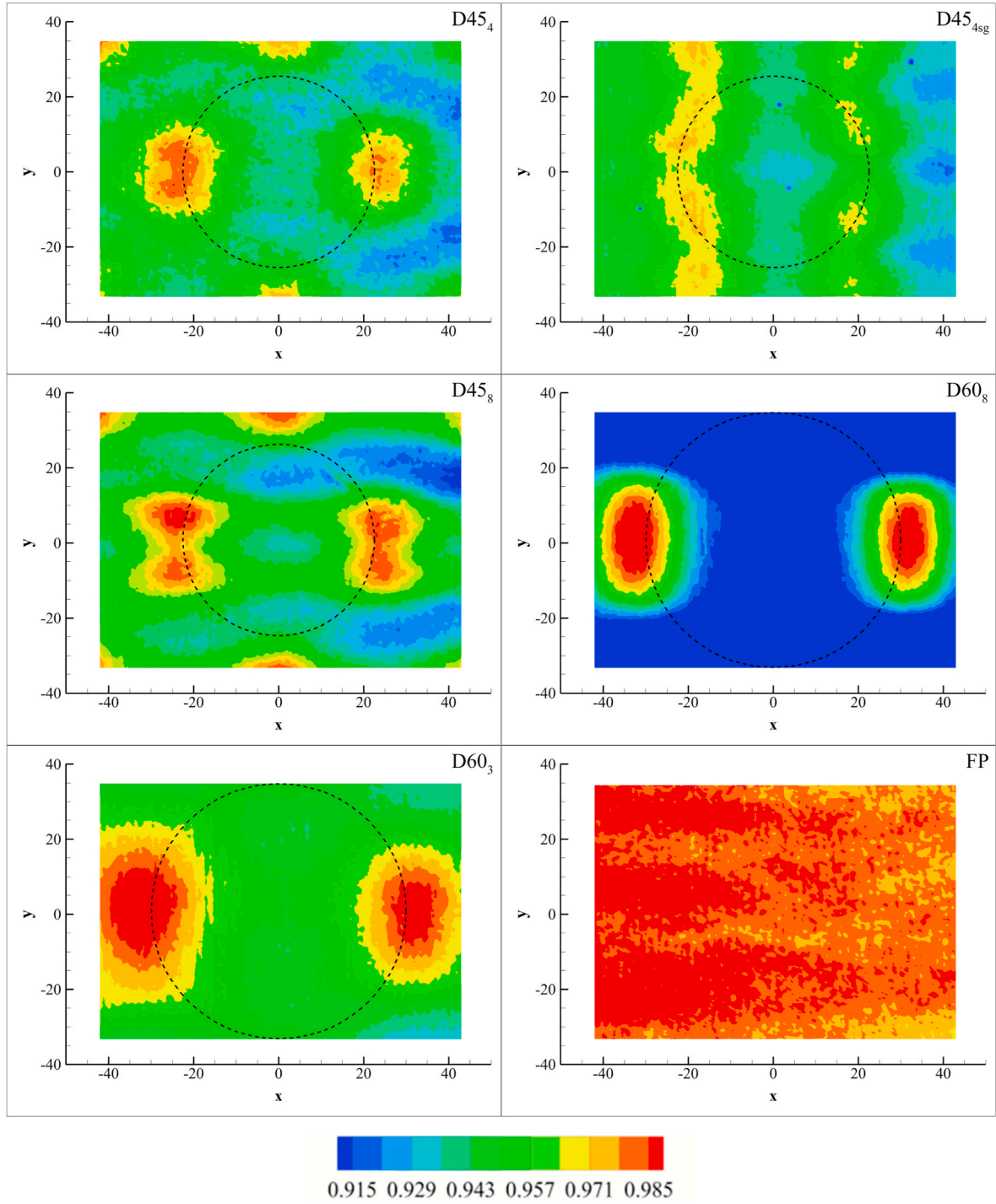


Fig. 19.  $\bar{u}/U_b$  distributions at 24 Hz pump frequency ( $U_b \cong 8.02$  m/s). The flow direction is from left to right.

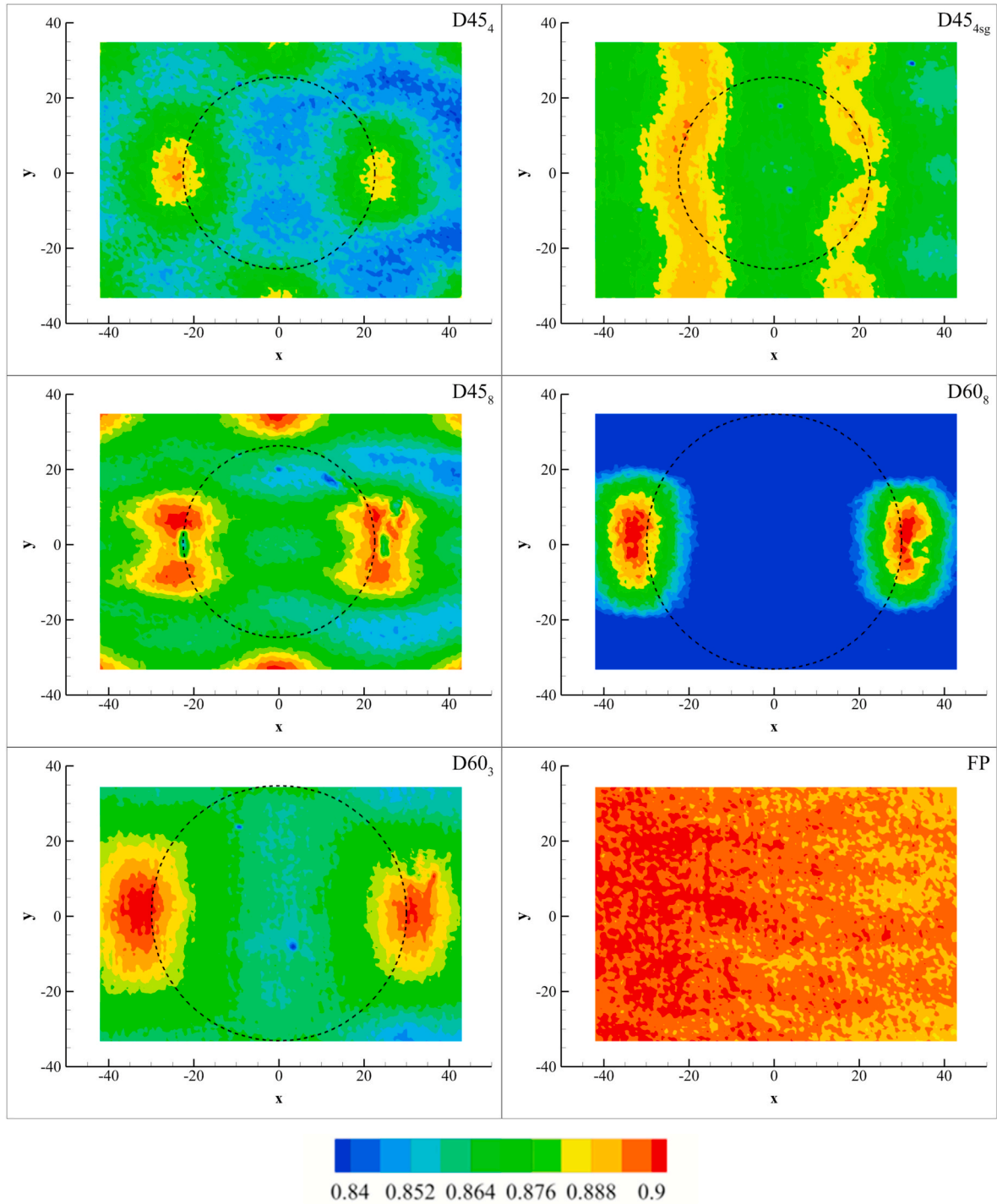


Fig. 20.  $\bar{u}/U_b$  distributions at 38 Hz pump frequency ( $U_b \cong 12.85$  m/s). The flow direction is from left to right.

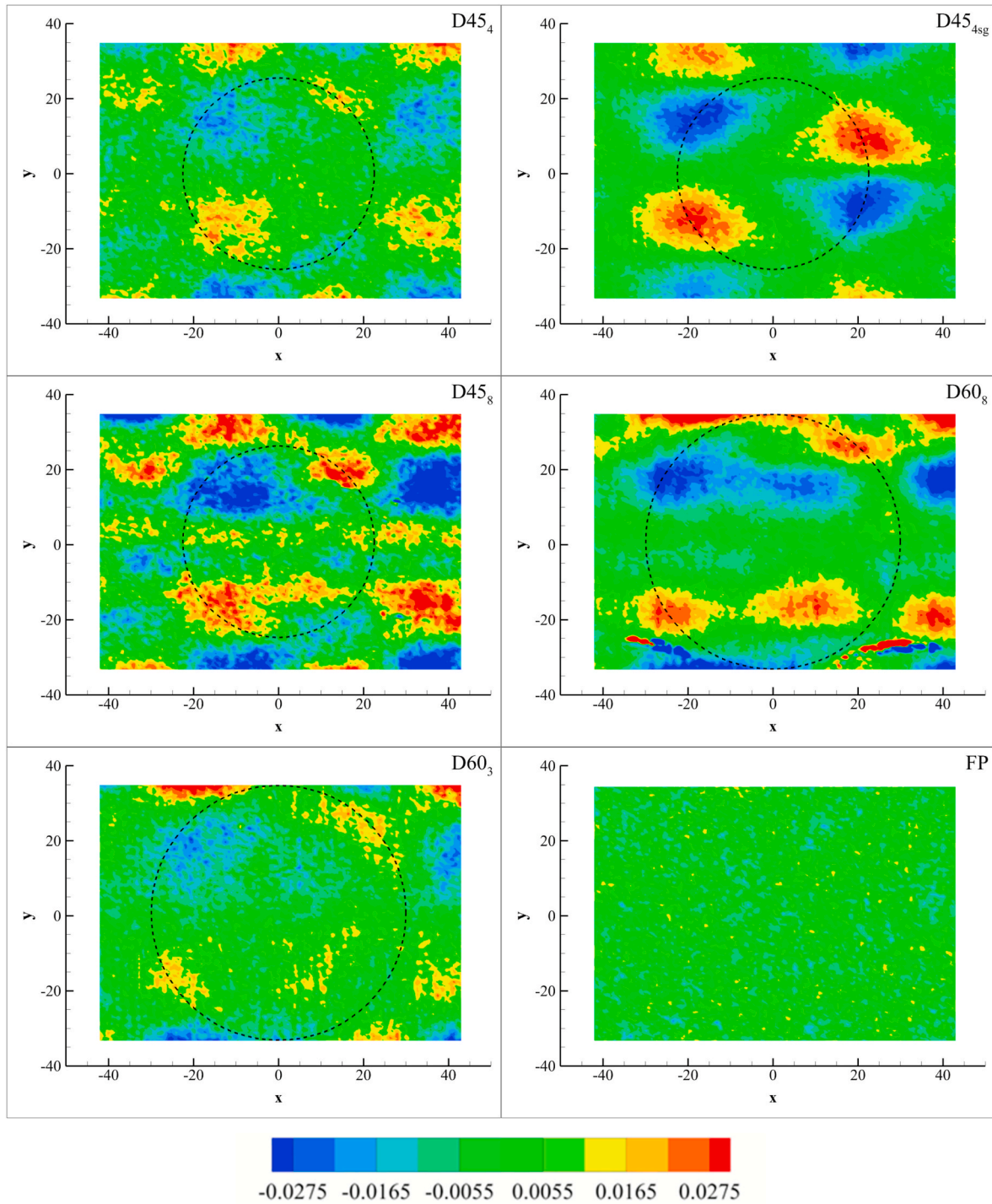


Fig. 21.  $\bar{w}/U_b$  distributions at 6 Hz pump frequency ( $U_b \cong 1.79$  m/s). The flow direction is from left to right.

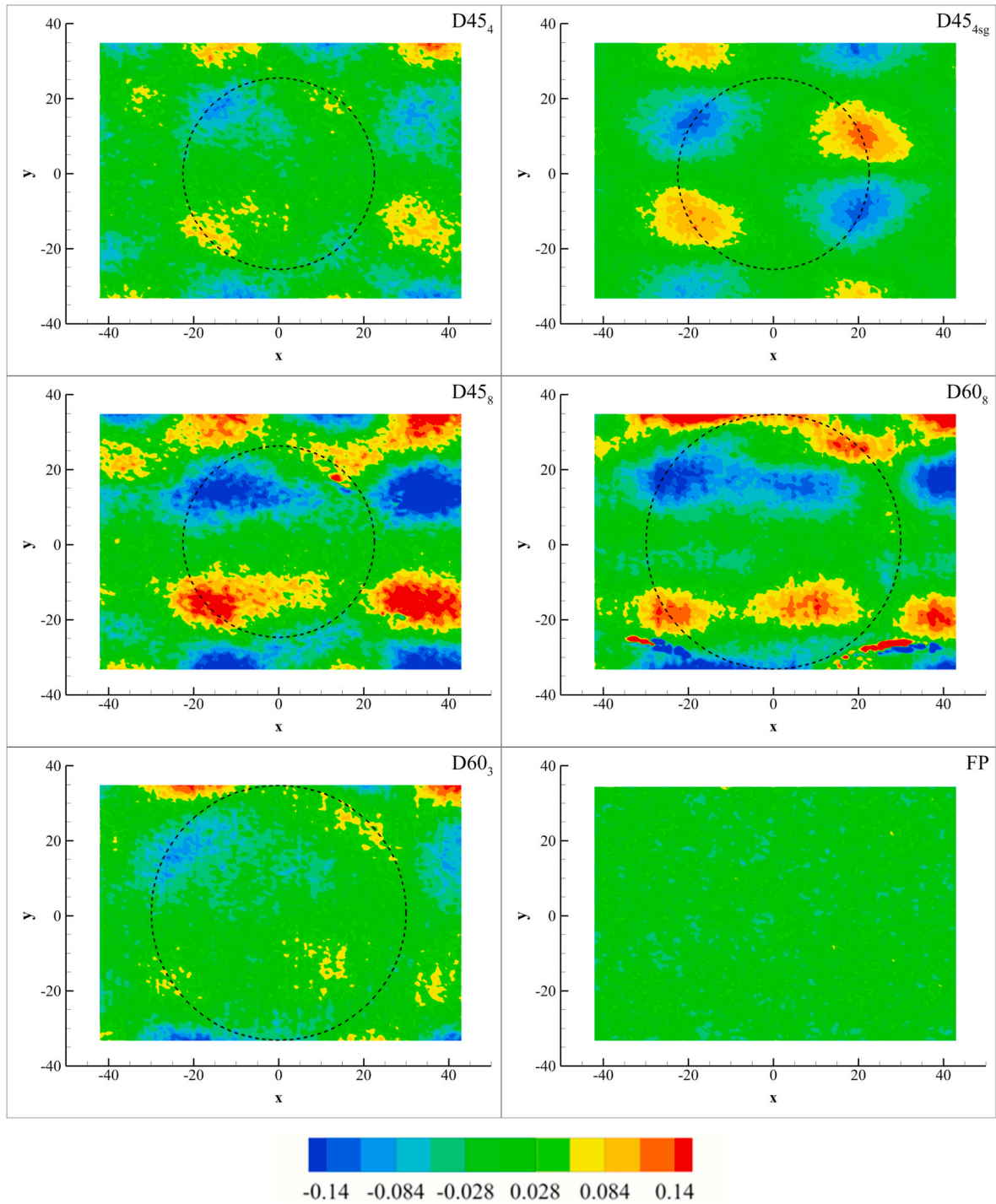


Fig. 22.  $\bar{w}/U_b$  distributions at 24 Hz pump frequency ( $U_b \cong 8.02 \text{ m/s}$ ). The flow direction is from left to right.

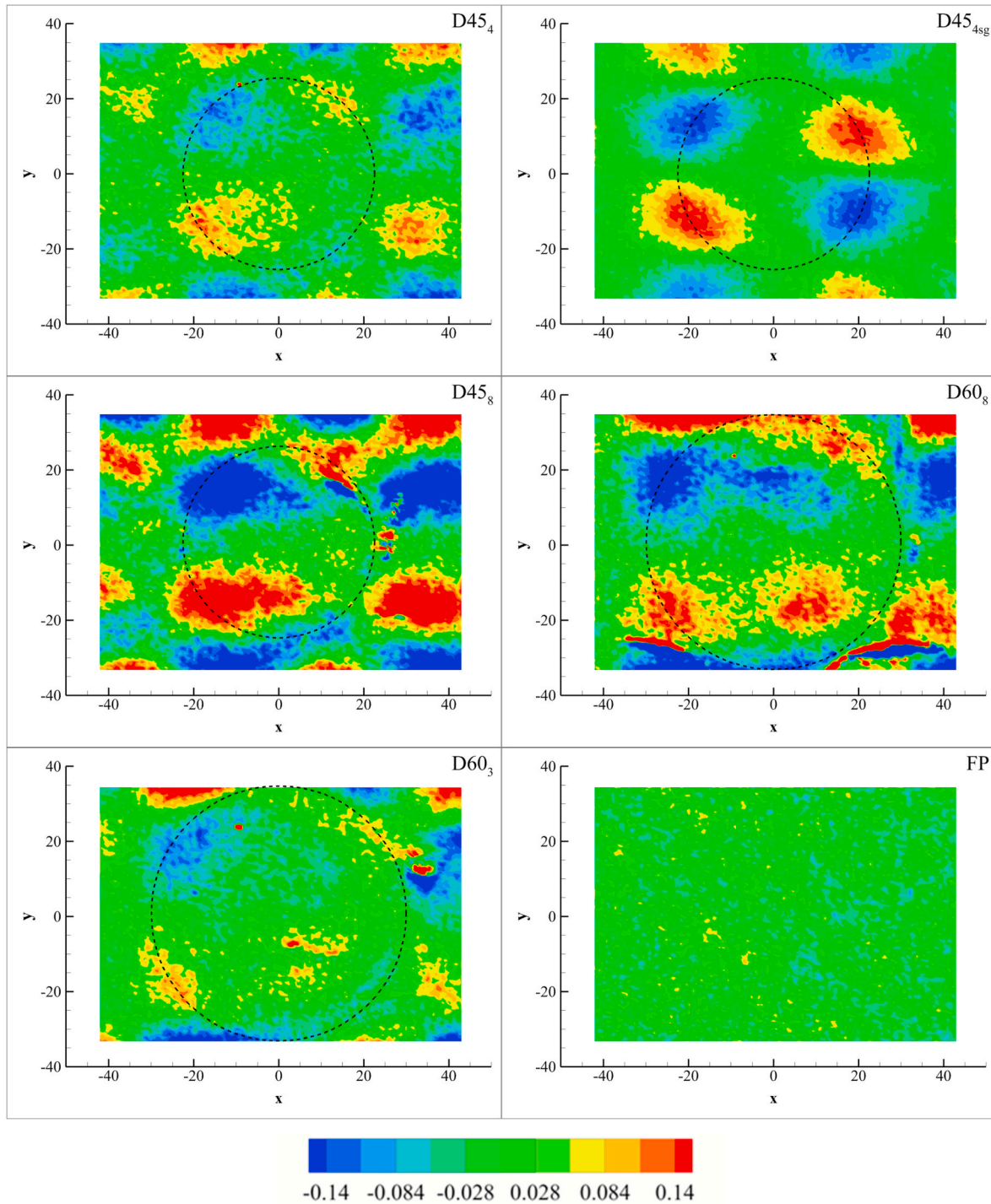


Fig. 23.  $\bar{w}/U_b$  distributions at 38 Hz pump frequency ( $U_b \cong 12.85 \text{ m/s}$ ). The flow direction is from left to right.

remained almost unchanged for the other bulk velocities tested, as depicted in Figs. 22 and 23. The plots suggest a correlation between the transverse velocity components and the resistance reduction performance of the dimpled plates. In other words, as the magnitude of the transverse velocity component decreases, the resistance also decreases. This behaviour is found to remain consistent for all three bulk velocities tested, as presented in Figs. 21–23. This implies that generating a transverse flow component without over-energising the flow in the same direction appears to be beneficial in terms of drag reduction (see İlter et al., 2023).

## 6. Conclusion

This work presented a comprehensive experimental investigation of the drag reduction performance of dimpled surfaces in a fully turbulent channel flow. The study employed pressure drop measurements and PIV visualisations to evaluate the effectiveness of various dimple configurations, including different depth-to-diameter ratios, diameters, and orientations.

The experimental results demonstrated that dimple geometries with relatively low depth-to-diameter ratios could achieve significant drag reduction rates of up to 27% as the Reynolds number based on channel

height ( $Re_H$ ) increased. This finding highlights the potential of dimpled structures to provide considerable energy savings in ship hull surfaces, where skin friction accounts for a significant portion of the total drag experienced by vessels. However, the measurements also revealed that specific dimple configurations could be strongly ineffective, emphasising the importance of optimising the geometric properties of the dimples to maximise their drag reduction capabilities.

The compatibility of the present findings with the previous numerical studies conducted by the authors enhances the reliability of the experimental data, supporting the use of dimpled surfaces as a viable passive drag-reduction technique. The agreement between the two approaches also suggests that both the experimental and computational methods effectively capture the underlying flow physics and drag reduction mechanisms, as well as complement each other's strengths.

The study demonstrated the benefits of channel flow experiments in dimple research while pointing out that several key factors should be considered when designing channel flow experiments to guide future research in this field. Firstly, the test section should be as long as possible, with pressure measurement points located both upstream and downstream to capture the full development of the flow. Secondly, alternative methods for directly quantifying skin friction resistance should be explored to complement the pressure drop measurements, including open-flow tests in large and high-speed water (cavitation) tunnels. Also, the use of high-frequency PIV or tomographic PIV systems to capture the three-dimensional flow structures and unsteady dynamics of flow over dimpled surfaces can provide further physical insights into the drag-reducing mechanism of dimple structures. While flow channel measurements provide very practical and valuable insights into the overall hydrodynamic performance, they may not capture the intricate flow details within the dimples due to limited visual access in the channel. Therefore, incorporating a range of measurements on large test plates in a water tunnel could offer a more comprehensive understanding of the effects of dimpled structures on skin friction resistance.

The present study is believed to highlight the significant potential of dimpled surfaces in reducing frictional resistance in turbulent flows. The experimental findings demonstrated the effectiveness of optimised dimple configurations in achieving substantial drag reduction. However, further experimental investigations are necessary to fully understand the benefits of dimpled surfaces in enhancing energy savings in maritime applications. By considering the recommendations outlined in this work, future research can build upon these findings and contribute to developing efficient and sustainable drag reduction solutions for the maritime industry.

#### CRedit authorship contribution statement

**Yasin Kaan İlter:** Writing – original draft, Visualization, Methodology, Investigation, Conceptualization. **Uğur Oral Ünal:** Writing – review & editing, Supervision, Resources, Methodology, Conceptualization. **Weichao Shi:** Supervision, Resources, Methodology, Investigation. **Sedat Tokgöz:** Visualization, Supervision, Methodology, Conceptualization. **Mehmet Atlar:** Writing – review & editing, Supervision, Resources, Project administration.

#### Declaration of competing interest

The authors declare the following financial interests/personal relationships which may be considered as potential competing interests:

Yasin Kaan İlter reports equipment, drugs, or supplies was provided by University of Strathclyde Naval Architecture Ocean and Marine Engineering. If there are other authors, they declare that they have no known competing financial interests or personal relationships that could have appeared to influence the work reported in this paper.

The pressure drops obtained exhibit a linear behaviour when plotted at the same  $x$  distances (Fig. 13). This indicates that the flow is fully turbulent. Numbers 1–6, 2–6, 3–6, 4–6, and 5–6 respectively represent

the tap configurations.

#### Data availability

Data will be made available on request.

#### Acknowledgement

We express our sincere thanks to the team at the Kelvin Hydrodynamics Laboratory for their invaluable assistance throughout this research adventure. Their proficiency, technical support, and provision of cutting-edge facilities, like the newly commissioned Fully Turbulent Flow Channel, have played a crucial role in the successful execution of our experiments.

We also express our gratitude to GÜRDESAN A.Ş. of Istanbul for their exceptional expertise in producing the test plates used in this study.

Additionally, the authors gratefully acknowledge the support and mentorship provided by Prof. Okşan Çetiner Yıldırım and Prof. Emin Korkut of Istanbul Technical University.

#### References

- Afanasyev, V.N., Chudnovsky, Y.P., Leontiev, A.I., Roganov, P.S., 1993. Turbulent flow friction and heat transfer characteristics for spherical cavities on a flat plate. *Exp. Therm. Fluid Sci.* 7 (1), 1–8.
- Alekseev, V.V., Gachechiladze, I.A., Kiknadze, G.I., Oleinikov, V.G., 1998. Tornado-like energy transfer on three-dimensional concavities of reliefs-structure of self-organizing flow, their visualisation, and surface streamlining mechanisms. *Transactions of the 2nd Russian Nat. Conf. of Heat Transfer, Heat Transfer Intensification Radiation and Complex Heat Transfer* 6, 33–42.
- Andrade, J.R., Martins, R.S., Mompean, G., Thais, L., Gatski, T.B., 2018. Analyzing the spectral energy cascade in turbulent channel flow. *Phys. Fluids* 30 (6). <https://doi.org/10.1063/1.5022653>.
- Burgess, N.K., Ligrani, P.M., 2005. Effects of dimple depth on channel nusselt numbers and friction factors. *J. Heat Tran.* 127 (8), 839. <https://doi.org/10.1115/1.1994880>.
- Chen, Y., Chew, Y.T., Khoo, B.C., 2012. Enhancement of heat transfer in turbulent channel flow over dimpled surface. *Int. J. Heat Mass Tran.* 55 (25–26), 8100–8121. <https://doi.org/10.1016/j.jlheatmasstransfer.2012.08.043>.
- Coleman, H.W., Glenn Steele, W., 1995. Engineering application of experimental uncertainty analysis. *AIAA J.* 33 (10) <https://doi.org/10.2514/3.12742>.
- Dean, R.B., 1978. Reynolds number dependence of skin friction and other bulk flow variables in two-dimensional rectangular duct flow. *J. Fluid Eng.* 100 (2), 215. <https://doi.org/10.1115/1.3448633>.
- Hussain, A.K.M.F., Reynolds, W.C., 1975. Measurements in fully developed turbulent channel flow. *J. Fluid Eng.* 97 (4), 568. <https://doi.org/10.1115/1.3448125>.
- İlter, Y.K., Çetinkaya, A., Unal, U.O., 2023. Large eddy simulations of the turbulent channel flow over dimpled surfaces. <https://doi.org/10.1080/14685248.2023.2186415>.
- Kim, J., Moin, P., Moser, R., 1987. Turbulence statistics in fully developed channel flow at low Reynolds number. *J. Fluid Mech.* 177, 133–166. <https://doi.org/10.1017/S0022112087000892>.
- Laufer, J., 1951. Investigation of turbulent flow two-dimensional channel. <https://ntrs.nasa.gov/search.jsp?R=19930092098>.
- Lienhart, H., Breuer, M., Köksoy, C., 2008. Drag reduction by dimples? – a complementary experimental/numerical investigation. *Int. J. Heat Fluid Flow* 29 (3), 783–791. <https://doi.org/10.1016/j.jlheatfluidflow.2008.02.001>.
- Ligrani, P.M., Harrison, J.L., Mahmood, G.I., Hill, M.L., 2001. Flow structure due to dimple depressions on a channel surface. *Phys. Fluids* 13 (11), 3442–3451. <https://doi.org/10.1063/1.1404139>.
- Marino, A., İlter, Y.K., Song, S., Shi, W., Atlar, M., Demirel, Y.K., 2020. Design specification, commission and calibration of the university of strathclyde's fully turbulent Flow Channel (FTFC) facility. *The Advanced Model Measurement Technology for the Maritime Industry* 136–147.
- Moser, R.D., Kim, J., Mansour, N.N., 1999. Direct numerical simulation of turbulent channel flow up to  $Re_\tau=590$ . *Phys. Fluids* 11 (4), 943–945. <https://doi.org/10.1063/1.869966>.
- Ng, J.H., Jaiman, R.K., Lim, T.T., Tay, C.M., Khoo, B.C., 2020. Geometric effects of shallow dimples in turbulent channel flows at  $Re_\tau \approx 180$ : a vorticity transport perspective. *Flow, Turbul. Combust.* 1–40. <https://doi.org/10.1007/s10494-020-00112-6>.
- Raffel, M., Willert, C.E., Scarano, F., Kähler, C.J., Wereley, S.T., Kompenhans, J., 2018. *Particle Image Velocimetry*, third ed. Springer International Publishing. <https://doi.org/10.1007/978-3-319-68852-7>.
- Sciacchitano, A., Wieneke, B., 2016. PIV uncertainty propagation. *Meas. Sci. Technol.* 27, 16. <https://doi.org/10.1088/0957-0233/27/8/084006>.
- Spalart, P.R., Shur, M., Strelets, M., Travin, A., Paschal, K.B., Wilkinson, S.P., 2019. Experimental and numerical study of the turbulent boundary layer over shallow dimples. *Int. J. Heat Fluid Flow* 78, 108438. <https://doi.org/10.1016/j.jheatfluidflow.2019.108438>.

- Tay, C.M.J., 2011. Determining the effect of dimples on drag in a turbulent channel flow. In: 49th AIAA Aerospace Sciences Meeting Including the New Horizons Forum and Aerospace Exposition. <https://doi.org/10.2514/6.2011-682>.
- Tay, C.M.J., 2016. Flow Past Dimpled Surfaces. National University of Singapore. <http://scholarbank.nus.sg/bitstream/10635/124186/1/TayCMJ.pdf>.
- Tay, C.M.J., Khoo, B.C., Chew, Y.T., 2015. Mechanics of drag reduction by shallow dimples in channel flow. *Phys. Fluids* 27 (3), 035109. <https://doi.org/10.1063/1.4915069>.
- 26th ITTC Specialist Committee on Uncertainty Analysis, 2011. Fresh water and seawater properties. *International Towing Tank Conference* 5 (10).
- Turnow, J., Kornev, N., Zhdanov, V., Hassel, E., 2012. Flow structures and heat transfer on dimples in a staggered arrangement. *Int. J. Heat Fluid Flow* 35, 168–175. <https://doi.org/10.1016/j.ijheatfluidflow.2012.01.002>.
- van Nesselrooij, M., Veldhuis, L.L.M., van Oudheusden, B.W., Schrijer, F.F.J., 2016. Drag reduction by means of dimpled surfaces in turbulent boundary layers. *Exp. Fluids* 57 (9), 142. <https://doi.org/10.1007/s00348-016-2230-9>.
- Veldhuis, L.L.M., Vervoort, E., 2009. Drag effect of a dented surface in a turbulent flow. In: *Collection of Technical Papers - AIAA Applied Aerodynamics Conference*. <https://doi.org/10.2514/6.2009-3950>.
- Vida, N., 2004. Three dimensional surface structure for reduced friction resistance and improved heat exchange. Patent No. US20070193726A1. <https://patents.google.com/patent/WO2004083651A1/en>.
- Westerweel, J., Scarano, F., 2005. Universal outlier detection for PIV data. *Exp. Fluids* 39 (6), 1096–1100. <https://doi.org/10.1007/s00348-005-0016-6>.
- Wu, J., Yeo, K.S., 2011. Flow past dimpled surfaces; Part 2: computational study for turbulent flow in dimpled channels. In: *Annual Report on the NUS-Airbus Collaboration under Project R-265-000-272*, p. 597.
- Wüst, C., 2004. Dellen im Dach. *Der Spiegel*, pp. 170–172. <http://magazin.spiegel.de/EpubDelivery/spiegel/pdf/30346859>.
- Zanoun, E.-S., Durst, F., Nagib, H., 2003. Evaluating the law of the wall in two-dimensional fully developed turbulent channel flows. *Phys. Fluids* 15 (10), 3079. <https://doi.org/10.1063/1.1608010>.